First light from a kilometer-baseline Scintillation Auroral GPS Array

S. Datta-Barua[1], Y. Su[1], K. Deshpande[2], D. Miladinovich[1], G. S. Bust[3], D. Hampton[4], and G. Crowley[5]

[1]Mechanical, Materials, and Aerospace Engineering Department, Illinois Institute of Technology, Chicago, Illinois, USA, [2]Bradley Department of Electrical and Computer Engineering, Virginia Polytechnic Institute and State University, Blacksburg, Virginia, USA, [3]Johns Hopkins University Applied Physics Laboratory, Laurel, Maryland, USA, [4]Geophysical Institute, University of Alaska Fairbanks, Fairbanks, Alaska, USA, [5]Atmospheric and Space Technology Research Associates, Boulder, Colorado, USA

Abstract We introduce and analyze the first data from an array of closely spaced Global Positioning System (GPS) scintillation receivers established in the auroral zone in late 2013 to measure spatial and temporal variations in L band signals at 100–1000 m and subsecond scales. The seven receivers of the Scintillation Auroral GPS Array (SAGA) are sited at Poker Flat Research Range, Alaska. The receivers produce 100 s scintillation indices and 100 Hz carrier phase and raw in-phase and quadrature-phase samples. SAGA is the largest existing array with baseline lengths of the ionospheric diffractive Fresnel scale at L band. With an initial array of five receivers, we identify a period of simultaneous amplitude and phase scintillation. We compare SAGA power and phase data with collocated 630.0 nm all-sky images of an auroral arc and incoherent scatter radar electron precipitation measurements, to illustrate how SAGA can be used in multi-instrument observations for subkilometer-scale studies.

1. Introduction

In the auroral zone, energetic particle precipitation in the upper atmosphere often leads to variations in plasma density from a few kilometers down to 100 m scale size. Poker Flat Research Range (PFRR), Alaska, is an important research site for investigating the dynamics of the high-latitude upper atmosphere. Operated by the University of Alaska at Fairbanks, PFRR hosts a suite of geospace sounding and sensing instruments including the Poker Flat Incoherent Scatter Radar (PFISR) [*Semeter et al.*, 2009], optical all-sky imagers (ASI) [*Hampton et al.*, 2013], scanning Doppler imagers [*Conde and Smith*, 1997; *Anderson et al.*, 2013], and a launch site for rocket sounding [*Zettergren et al.*, 2014]. Most of these instruments make measurements at about 10–100 km scales or in situ point measurements.

However, the subkilometer-scale ionospheric irregularities can cause scintillation, short-term signal fading, and rapid variations in the phase of transionospheric signals, from Global Navigation Satellite Systems (GNSS) such as the Global Positioning System (GPS). At high latitudes, phase scintillations are observed more often than amplitude scintillations and are due to a variety of physical instability mechanisms in both the *E* and *F* regions of the ionosphere. The temporal behavior of diffractive scintillations depends on the Fresnel length of the scintillations, the drift speed of the ionosphere, and the relative velocities of the satellites and receivers [*Kintner et al.*, 2004].

There have been a number of significant high-latitude studies of scintillation using GPS [*Mitchell et al.*, 2005; *Skone et al.*, 2009; *Grzesiak and Wernik*, 2009; *Prikryl et al.*, 2010; *Alfonsi et al.*, 2011; *Wang et al.*, 2012]. Most GPS high-latitude scintillation studies were made with single scintillation receivers or a network with baselines of one to hundreds of kilometers and, therefore, were not able to investigate the local spatial spectrum of the irregularities or the drift speeds.

Until recently, there was no dedicated scintillation monitoring array at PFRR and none operating routinely at subkilometer baselines anywhere. We present our installation and systematic data collection, processing, and sharing system for study of the spatial-temporal properties of GPS scintillations at high latitudes using a closely spaced multireceiver array deployed in the northern auroral zone: the Scintillation Auroral GPS Array (SAGA).
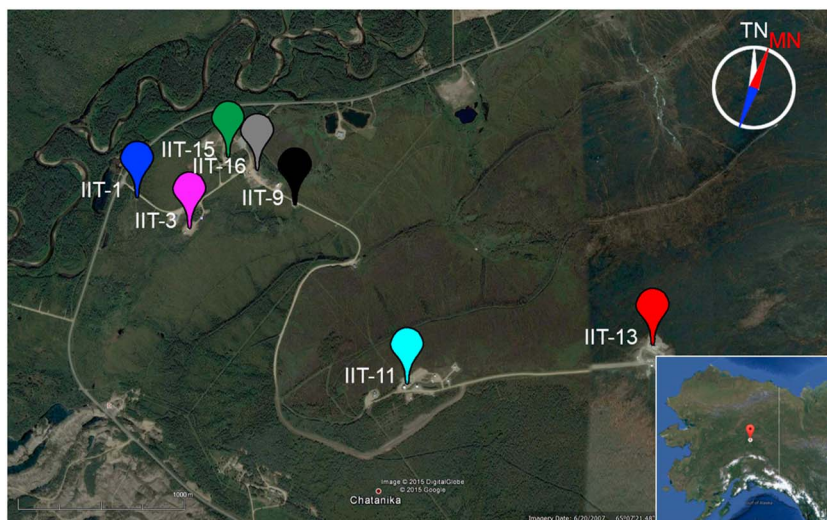
Figure 1. Map of array location with true north (TN) to the top (courtesy of Google Maps). Red compass arrow indicates magnetic north (MN). Pin colors correspond to the curves that will be used in Figure 5 later. Inset: Alaska.

2. Scintillation Auroral GPS Array

The purpose of SAGA is to quantify the two-dimensional space-time distribution of scintillations and the ionospheric irregularities that produce them, connecting them to the time history of auroral structuring, larger-scale electron gradients, electrodynamics, and winds. Atmospheric and Space Technology Research Associates (ASTRA) Connected Autonomous Space Environment Sensors (CASES) receivers [*Crowley et al.*, 2011; *O'Hanlon et al.*, 2011] based on technology by *Humphreys et al.* [2010] are used. The six receivers established by the team are located at the westernmost sites identified on the map of PFRR in Figure 1. Each has a site ID ("IIT-") labeled on the map. In addition, ASTRA has a receiver at the site marked in red, for a total of seven receivers in the array. Table 1 summarizes the configuration at the present time. The array is spaced over the ground in two dimensions, with 200 m to 3100 m baselines.

Each scintillation monitor is a software-based receiver connected to an external antenna on the roof of the building site and is powered and networked with a basic Linux operating system interface. The data types collected fall into three categories: scintillation indices with a cadence of 100 s, low rate with a cadence of 1 s, and high rate with a cadence of 0.01 s. The indices include calculated parameters of amplitude and phase scintillation $S4$ and σ_ϕ, decorrelation time τ_0, and scintillation power ratio (SPR). $S4$ and σ_ϕ are the normalized standard deviation of signal intensity and phase, respectively, computed over 100 s intervals as currently configured. The decorrelation time τ_0 is the time shift for which the autocorrelation of the time-varying multipath drops by $1/e$ [*Humphreys et al.*, 2009]. The SPR computes the ratio of spectral power in a user-selected narrow band to the total power measured, primarily used for selective high-rate data collection in power- or storage-constrained environments [*O'Hanlon et al.*, 2011]. The low-rate data includes typical GPS observables such as pseudorange and carrier phase, receiver position, satellite IDs (PRNs) tracked, azimuth and elevation angle, and calculated total electron content (TEC). The high-rate data include carrier phase, as well as in-phase (I) and quadrature-phase (Q) accumulations.

The scintillation and low-rate data are streamed in binary format over the network to a server database. The

Table 1. SAGA Receiver Locations, in WGS-84 Coordinates

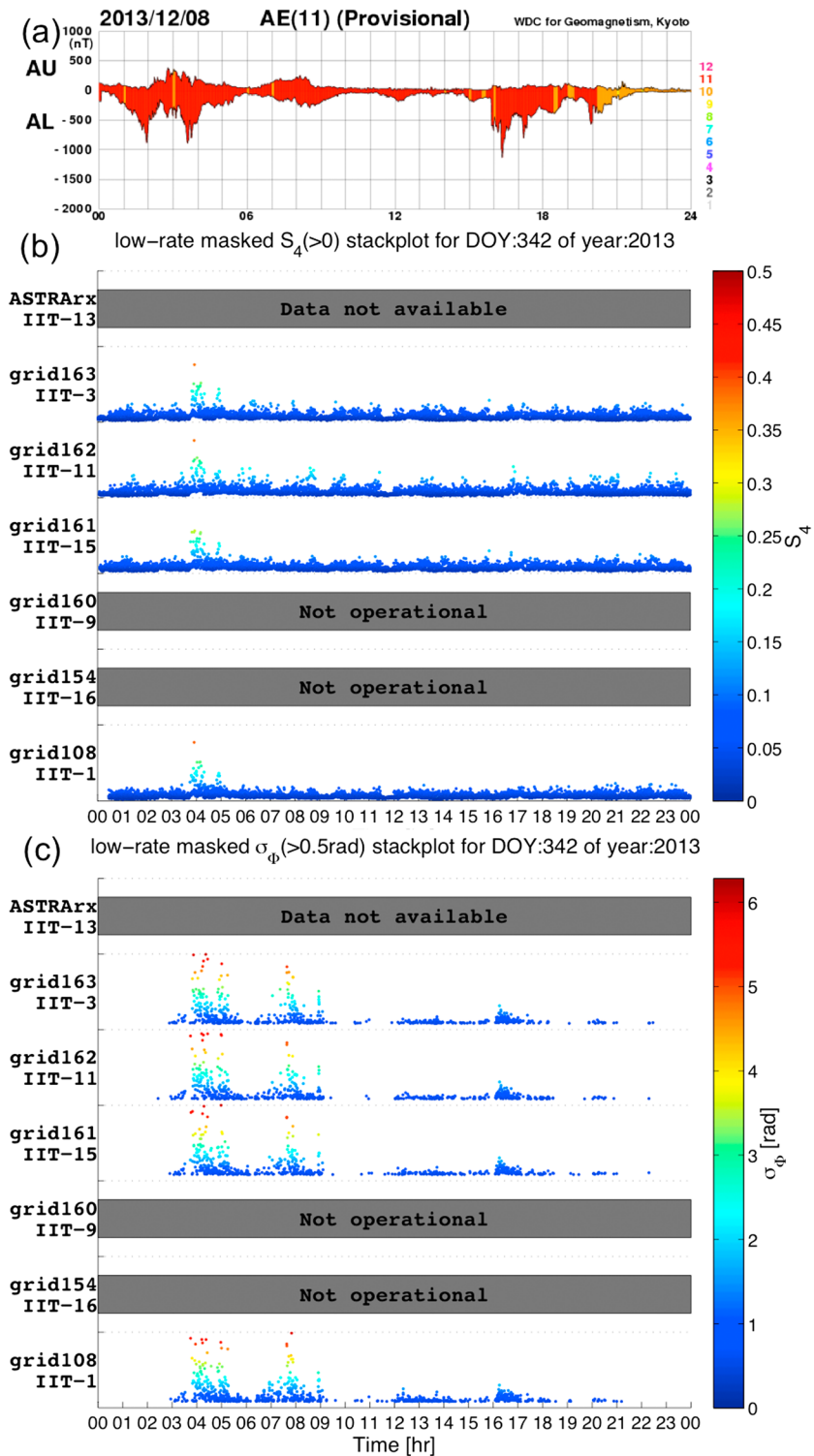| Site ID	Receiver ID	Latitude (°N)	Longitude (°E)	Height (m)
IIT-1	GRID108	65.1265	−147.4968	210
IIT-3	GRID163	65.1248	−147.4900	210
IIT-9	GRID160	65.1262	−147.4767	211
IIT-11	GRID162	65.1169	−147.4623	422
IIT-13	ASTRA rx[a]	65.1186	−147.4329	519
IIT-15	GRID161	65.1287	−147.4853	212
IIT-16	GRID154	65.1279	−147.4815	208

[a]Not available as part of the online database.

Figure 2. The 8 December 2013 (a) *AE* indices [*World Data Center for Geomagnetism, Kyoto*, 2014], (b) SAGA *S4* index, and (c) SAGA σ_ϕ QuickLook plots. Color and vertical scale of Figure 2b both indicate *S4* value to emphasize scintillating periods. Likewise for Figure 2c.
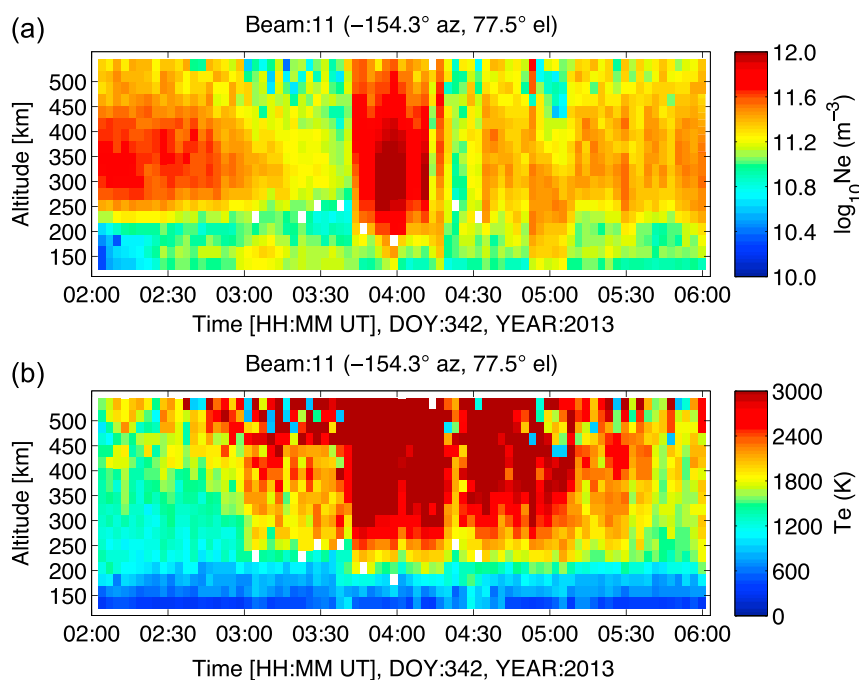
Figure 3. PFISR electron density N_e and temperature T_e measurements versus time and altitude for the beam nearest to the raypath between PRN 23 and SAGA.

database is searchable by a web interface for viewing and downloading, publicly available at http://apollo.tbc.iit.edu/~spaceweather.

The streamed data are processed daily to generate QuickLook plots and test for potential scintillation events. Phase scintillation index values from each receiver are filtered to mask satellites below 30° elevation. Then the σ_ϕ values below a manually predefined threshold (currently 0.5 rad, almost 3 times the quiet-time average σ_ϕ) are discarded. The results are plotted on the website as "QuickLook" plots.

The scintillation indices are used to identify time periods of interest, but detailed analyses with SAGA rely on the high-rate data. Time intervals during which σ_ϕ exceeds a higher threshold are recorded (currently set to one standard deviation above the average σ_ϕ for the given day). For these start and end time intervals, the high-rate data for the corresponding whole hour are downloaded from the receivers. The high-rate data are unpacked from binary into text format, to be used for scientific analyses.

For individual studies, the 100 Hz high-rate phase data are processed as detailed by *Deshpande et al.* [2012]. These filtering methods are consistent with the standard methods of filtering high-rate GNSS observations as described by *van Dierendonck and Hua* [2001]. At present, to remove the receiver clock errors, carrier and IQ phase of a nonscintillating reference channel are subtracted from those of a possibly scintillating channel. The differenced carrier phase ϕ_c and the differenced IQ phase ϕ_{iq} are then added together to obtain the sum phase ϕ. A third-order polynomial fit $\tilde{\phi}$ of phase ϕ is subtracted to remove satellite geometry effects and obtain phase ϕ' with mostly high-frequency components. A high-pass sixth-order Butterworth filter with cutoff frequency 0.1 Hz for data intervals longer than 60 s (or 0.2 Hz otherwise) then removes any residual low-frequency components from ϕ' and produces the final detrended phase ϕ_f. To detrend power, the raw power P_r of a scintillating PRN is filtered by a sixth-order low-pass Butterworth filter to obtain a low-pass-filtered output P_{LPF}. Dividing P_r by P_{LPF} produces the high-pass-filtered power P_f. We use standard filtering techniques to generate scintillation indices and in our current analysis, but there are other methods yielding alternate indices [*Mushini et al.*, 2012]. With the high-rate data available from SAGA, future studies may investigate alternate filtering methods.

3. Sample Results

An example of the scintillation indices is shown in Figure 2. Figure 2a is a plot of the Provisional *AE* Indices provided by the *World Data Center for Geomagnetism, Kyoto* [2014]. Figures 2b and 2c show the scintillation
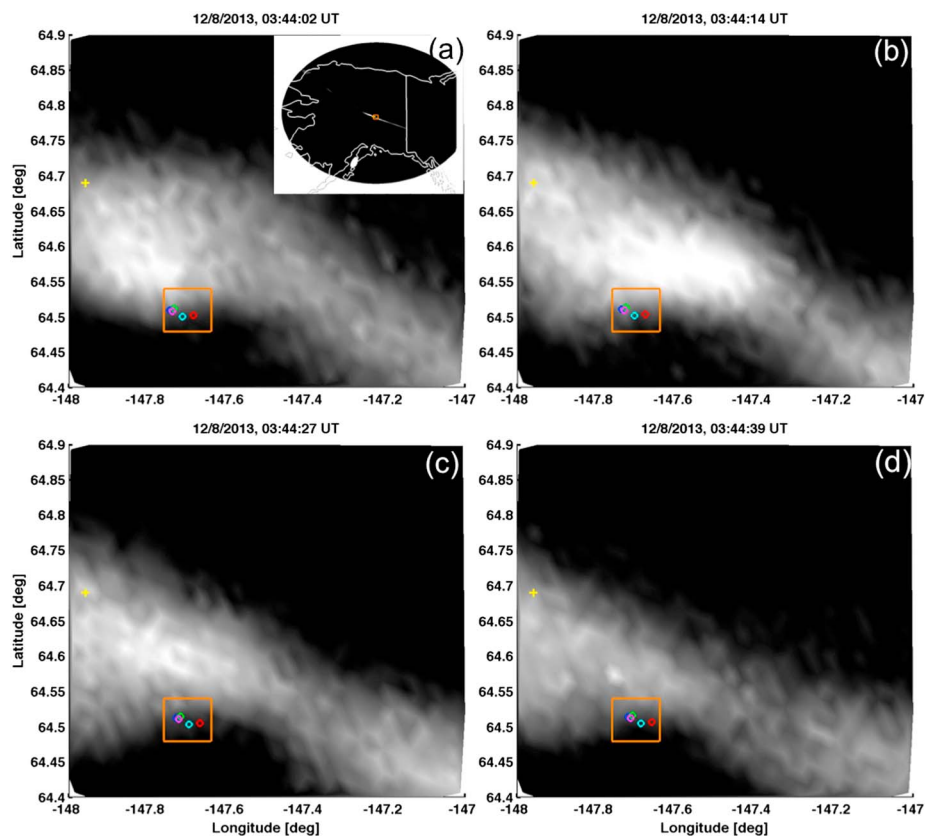
Figure 4. ASI 630.0 nm emission auroral images and SAGA array PRN 23 ionospheric pierce points (IPPs) mapped to 250 km altitude. Inset in Figure 4a shows full image over Alaska. (a) 03:44:02 UT, (b) 03:44:14 UT, (c) 03:44:27 UT, and (d) 03:44:39 UT. PFISR beam at 250 km shown as a yellow cross. Orange boxes are shown for emphasis.

measurements $S4$ and σ_ϕ from each of the six publicly available receivers that were operational at the time. The color scales in Figures 2b and 2c are mapped to the vertical axis values to emphasize elevated scintillation.

On 8 December 2013 there was a geomagnetic storm due to a corotating interaction region in the solar wind and coronal hole high-speed stream [*Space Weather Prediction Center*, 2013]. The Provisional AE index reprinted in Figure 2a from *World Data Center for Geomagnetism, Kyoto* [2014] shows periods of geomagnetic disturbance from 00:00 to 05:00 UT, 07:00 to 09:00 UT, and 16:00 to 20:00 UT. Elevated σ_ϕ scintillation activity in Figure 2c corresponds to the periods of activity denoted by the AE index, with the exception of 00:00–02:00 UT. Notably, Figure 2b shows there is significant amplitude scintillation ($S4 = 0.4$) close to 04:00 UT.

This date occurred during a PFISR Ion-Neutral Observations of the Thermosphere (PINOT) campaign [*Makarevich and Bristow*, 2014]. Figure 3 shows the PFISR electron density N_e and temperature T_e data for the beam nearest in the sky to the scintillating GPS signal that will be studied, from 02:00 UT to 06:00 UT. In Figure 3a a significant density enhancement is measured from 03:45 to 04:15 UT at altitudes above 200 km. For this same time through an hour later, high electron temperatures are measured at the F region altitudes. The measurements from PFISR indicate soft electron precipitation at F region altitudes.

The all-sky imager (ASI) at Poker Flat operates during nighttime from August to April and included this night. Correlation between auroral structuring and scintillation has been reported before [*Little and Maxwell*, 1952; *Smith et al.*, 2008; *Garner et al.*, 2011; *Hampton et al.*, 2013], but we illustrate this event in detail. Figures 4a–4d show consecutive 1 s exposures taken of the 630.0 nm (red line) emission with the ASI during the onset of significant scintillation at 03:44:02, 03:44:14, 03:44:27, and 03:44:39 UT. The ASI pixels are mapped to latitude and longitude locations assuming that the red-line emission takes place at 250 km altitude. The map inset in Figure 4a shows the full region imaged over Alaska with a small orange box showing the area of detail. The white spot to the southwest of the imaged area in the inset is light contamination from the moon. Each subplot zooms in on the image within a 1° longitude and 0.5° latitude span. The raw uncalibrated intensities
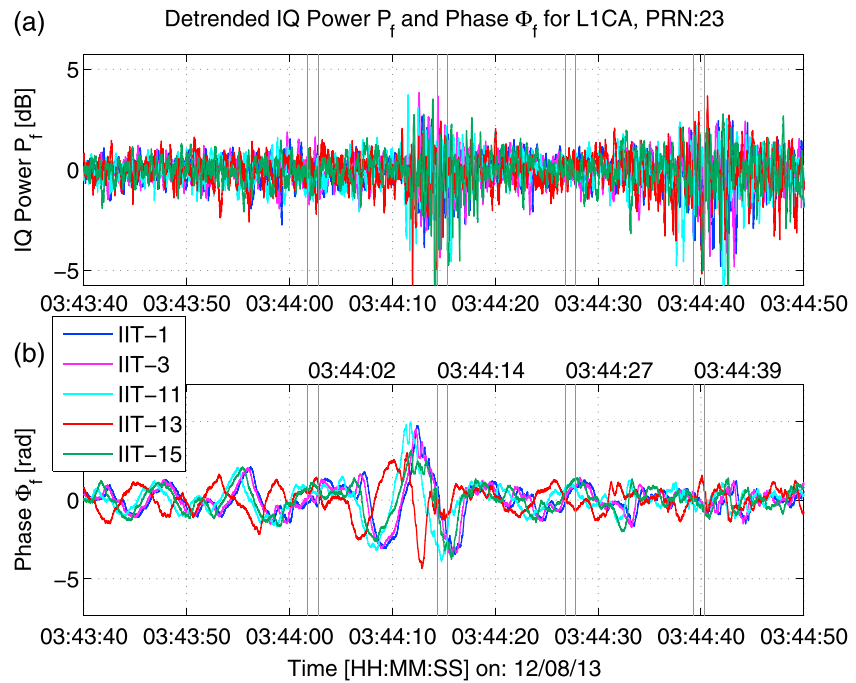
Figure 5. (a) I- and Q-based detrended power. (b) Final phase after detrending and filtering ϕ_f from 03:43:40 to 03:44:50 UT at 100 Hz. Time intervals of the ASI data of Figure 4 are marked.

are plotted in grayscale. In each map, the ionospheric pierce point (IPP) at 250 km altitude for the raypath of the signal from PRN 23 received by each SAGA receiver is shown as a colored circle. An orange box surrounds the SAGA IPPs for visual emphasis. A yellow cross marks the location of the nearest PFISR beam passing through 250 km altitude, whose data were shown in Figure 3. Though not visible at this level of zoom, the three closest operational SAGA sites' raypaths (IIT-1, IIT-3, and IIT-15) fall within one pixel of the ASI image.

An auroral arc is visible stretching from northwest to southeast. In every instant the PFISR beam appears to be passing right through the auroral arc. At 03:44:02 UT, the SAGA IPPs are just to the south of the arc. Twelve seconds later (Figure 4b), the arc brightens, and the IPPs seem to be on the southern edge of it. The bright area has faded significantly by 03:44:27 UT, such that the arc appears to retreat slightly northward away from the IPPs (Figure 4c). In the last image, Figure 4d, the arc has faded further with the IPPs still appearing to the south of the southern edge.

Figures 5a and 5b, respectively, show SAGA 100 Hz detrended I and Q power and detrended filtered phase [*Deshpande et al.*, 2012] from 03:43:40 UT to 03:44:50 UT. The colors of the curves correspond to the markers in the map of Figure 1 and to the IPPs shown in Figure 4. The time intervals during which red-line ASI exposures were taken are indicated with vertical lines. During this time, amplitude scintillation occurs, as seen by the increased variance in the signal power in Figure 5a at 03:44:12 and 03:44:40 UT. In the 70 s time interval of Figure 5b, variations in the signal phase received across the array become more clearly visible at about 03:44:12 UT, simultaneous with one interval of amplitude scintillation but not the other.

Consider the 5 rad peak in I and Q phase that occurs around 03:44:12 UT. Each of the curves is similar to each other but time shifted. From the map, it can be observed that the receivers that are collinear on a northwest-southeast axis (sites 13 and 15; sites 1, 3, and 11) have almost identical time series. This orientation aligns with the arc edge. Notably, both Figures 4b and 4d were taken during amplitude scintillation periods, but the one simultaneous with the significant phase variation (Figures 4b) showed a brightening of the arc while the one without phase scintillation did not (Figures 4d).

The phase measurements are time correlated and somewhat spatially correlated. The former feature allows us to estimate irregularity drift velocities projected along the direction of motion of the IPPs. Cross-correlation analyses between pairs of receivers have been done [*Datta-Barua et al.*, 2014] using methods described by *Basu et al.* [1991] and *Costa et al.* [1997]. Our initial estimate of the ionospheric drift velocity based on SAGA

measurements is a northwestward motion of about 1100 m/s. Comparisons with PFISR velocities show good agreement. A quantitative analysis of the time period shown in Figures 5a and 5b has been carried out using a Rytov approximation, and both the cross-correlation analysis and quantitative analysis are the subject of a forthcoming paper in preparation. While a detailed description of that analysis is beyond the scope of this current paper, the methods are based on *Yeh and Liu* [1982] and *Taylor* [1975]. The results of that analysis produced estimations of statistical properties of the irregularities including the following: a spectral index estimate of ~ 3.2; the standard deviation of irregularity density of $\sim 1.0 \times 10^{11} e/m^3$; a thickness of the irregularity layer of ~ 200 km; and the top of the irregularity layer located at ~ 500 km altitude. These results are consistent with the PFISR observations in Figure 3 and indicate that the scintillations may be due to soft *F* region electron precipitation. In this case the red-line auroral arc observations may be interpreted as originating from the bottom of the precipitation region.

4. Conclusion

Since the end of 2013, the largest existing array of seven closely spaced GPS L1/L2C scintillation monitors has been established at PFRR. Six of these provide ionospheric scintillation parameters and position estimates routinely, available to the public. For the event shown, an auroral arc crossing the raypath of the GPS L1 signal appears to be related to scintillation, with interreceiver phase similarities corresponding to the northwest-southeast orientation of the arc. There are two instances of significant power fluctuation, one with and one without phase scintillation, not usually correlated with arcs. Investigation with PFISR data is ongoing, and a detailed, quantitative study of this event will be the subject of a follow-on paper, obtaining two-dimensional drift velocities, spectral index, irregularity density distribution, and thickness of the irregularity layer. Used in conjunction with the complementary instruments and sensors collocated at PFRR, the SAGA data provide an unprecedented high-resolution view of the effects of auroral processes on GPS phase measurements.

References

Alfonsi, L., L. Spogli, G. D. Franceschi, V. Romano, M. Aquino, A. Dodson, and C. N. Mitchell (2011), Bipolar climatology of GPS ionospheric scintillation at solar minimum, *Radio Sci.*, *46*, RS0D05, doi:10.1029/2010RS004571.

Anderson, C., M. J. Kosch, M. J. Nicolls, and M. Conde (2013), Ion-neutral coupling in Earth's thermosphere, estimated from concurrent radar and optical observations above Alaska, *J. Atmos. Sol. Terr. Phys.*, *105*, 313–324, doi:10.1016/j.jastp.2013.04.005.

Basu, S., S. Basu, E. Costa, C. Bryant, C. E. Valladares, and R. C. Livingston (1991), Interplanetary magnetic field control of drifts and anisotropy of high-latitude irregularities, *Radio Sci.*, *26*(4), 1079–1103.

Conde, M., and R. W. Smith (1997), Phase compensation of a separation scanned, all-sky imaging Fabry-Perot spectrometer for auroral studies, *Appl. Opt.*, *36*(22), 5441–5450.

Costa, E., S. Basu, R. C. Livingston, and P. Stubbe (1997), Multiple baseline measurements of ionospheric scintillation induced by high-power HF waves, *Radio Sci.*, *32*(1), 191–197.

Crowley, G., G. S. Bust, A. Reynolds, I. Azeem, R. Wilder, B. W. O'Hanlon, M. L. Psiaki, S. Powell, T. E. Humphreys, and J. A. Bhatti (2011), CASES: A novel low-cost ground-based dual-frequency GPS software receiver and space weather monitor, in *Proceedings of the 24th International Technical Meeting of The Satellite Division of the Institute of Navigation (ION GNSS 2011)*, pp. 1437–1446, Inst. of Navig., Portland, Oreg.

Datta-Barua, S., Y. Su, K. Deshpande, G. S. Bust, and D. Hampton (2014), Auroral scintillation phase analysis from a short-baseline GPS array, in *Proceedings of the 27th International Technical Meeting of The Satellite Division of the Institute of Navigation (ION GNSS+ 2014)*, pp. 1101–1107, Inst. of Navig., Tampa, Fla.

Deshpande, K. B., G. S. Bust, C. R. Clauer, H. Kim, J. E. Macon, T. E. Humphreys, J. A. Bhatti, S. B. Musko, G. Crowley, and A. T. Weatherwax (2012), Initial GPS scintillation results from CASES receiver at South Pole, Antarctica, *Radio Sci.*, *47*, RS5009, doi:10.1029/2012RS005061.

Garner, T. W., R. B. Harris, J. A. York, C. S. Herbster, C. F. Minter III, and D. L. Hampton (2011), An auroral scintillation observation using precise, collocated GPS receivers, *Radio Sci.*, *46*, RS1018, doi:10.1029/2010RS004412.

Grzesiak, M., and A. W. Wernik (2009), Dispersion analysis of spaced antenna scintillation measurement, *Ann. Geophys.*, *27*, 2843–2849.

Hampton, D. L., S. I. Azeem, G. Crowley, J. Santana, and A. Reynolds (2013), GPS phase scintillation correlated with auroral forms, Abstract SA12A-02 presented at 2013 Fall Meeting, AGU, San Francisco, Calif.

Humphreys, T. E., M. L. Psiaki, J. C. Hinks, B. O'Hanlon, and J. P. M. Kintner (2009), Simulating ionosphere-induced scintillation for testing GPS receiver phase tracking loops, *IEEE J. Sel. Top. Sign. Proces.*, *3*(4), 707–715, doi:10.1109/JSTSP.2009.2024130.

Humphreys, T. E., M. L. Psiaki, B. M. Ledvina, A. P. Cerruti, and J. P. M. Kintner (2010), A data-driven testbed for evaluating GPS carrier tracking loops in ionospheric scintillation, *IEEE Trans. Aerosp. Electron. Syst.*, *46*, 1609–1623.

Kintner, P. M., B. M. Ledvina, E. R. de Paula, and I. J. Kantor (2004), Size, shape, orientation, speed, and duration of GPS equatorial anomaly scintillations, *Radio Sci.*, *39*, RS2012, doi:10.1029/2003RS002878.

Little, C. G., and A. Maxwell (1952), Scintillation of radio stars during aurorae and magnetic storms, *J. Atmos. Terr. Phys.*, *2*, 356–360.

Makarevich, R. A., and W. A. Bristow (2014), Coordinated radar observations of plasma wave characteristics in the auroral *F* region, *Ann. Geophys.*, *32*(7), 875–888, doi:10.5194/angeo-32-875-2014.

Mitchell, C. N., L. Alfonsi, G. D. Franceschi, M. Lester, V. Romano, and A. W. Wernik (2005), GPS TEC and scintillation measurements from the polar ionosphere during the October 2003 storm, *Geophys. Res. Lett.*, *32*, L12S03, doi:10.1029/2004GL021644.

Mushini, S. C., P. T. Jayachandran, R. B. Langley, J. W. MacDougall, and D. Pokhotelov (2012), Improved amplitude- and phase-scintillation indices derived from wavelet detrended high-latitude GPS data, *GPS Solutions*, *16*, 363–373, doi:10.1007/s10291-011-0238-4.

O'Hanlon, B. W., M. L. Psiaki, S. Powell, J. A. Bhatti, T. E. Humphreys, G. Crowley, and G. S. Bust (2011), CASES: A smart, compact GPS software receiver for space weather monitoring, in *Proceedings of the 24th International Technical Meeting of The Satellite Division of the Institute of Navigation (ION GNSS 2011)*, pp. 2745–2753, Inst. of Navig., Portland, Oreg.

Prikryl, P., P. T. Jayachandran, S. C. Mushini, D. Pokhotelov, J. W. MacDougall, E. Donovan, E. Spanswick, and J.-P. St-Maurice (2010), GPS TEC, scintillation and cycle slips observed at high latitudes during solar minimum, *Ann. Geophys.*, *28*(6), 1307–1316, doi:10.5194/angeo-28-1307-2010.

Semeter, J., T. Butler, C. Heinselman, M. Nicolls, J. Kelly, and D. Hampton (2009), Volumetric imaging of the auroral ionosphere: Initial results from PFISR, *J. Atmos. Sol. Terr. Phys.*, *71*(6-7), 738–743, doi:10.1016/j.jastp.2008.08.014.

Skone, S., M. Feng, R. Tiwari, and A. Coster (2009), Characterizing ionospheric irregularities for auroral scintillations, in *Proceedings of the 22rd International Technical Meeting of the Satellite Division of the Institute of Navigation (ION GNSS 2009)*, pp. 2551–2558, Inst. of Navig., Savannah, Ga.

Smith, A. M., C. N. Mitchell, R. J. Watson, R. W. Meggs, P. M. Kintner, K. Kauristie, and F. Honary (2008), GPS scintillation in the high Arctic associated with an auroral arc, *Space Weather*, *6*, S03D01, doi:10.1029/2007SW000349.

Space Weather Prediction Center (2013), Space weather highlights 02 December–08 December 2013, *Tech. Rep. SWPC PRF 1997*, Natl. Oceanic and Atmos. Admin., Boulder, Colo.

Taylor, L. S. (1975), Effects of layered turbulence on oblique waves, *Radio Sci.*, *10*(1), 121–128.

van Dierendonck, A. J., and Q. Hua (2001), Measuring ionospheric scintillation effects from GPS signals, in *Proceedings of the ION 57th Annual Meeting/CIGTF 20th Biennial Guidance Test Symposium*, pp. 391–396, Inst. of Navig., Albuquerque, N. M.

Wang, J., Y. Morton, Q. Zhou, and W. Pelgrum (2012), Spatial characterization of high latitude ionosphere scintillations, in *Proceedings of the 25th International Technical Meeting of The Satellite Division of the Institute of Navigation (ION GNSS 2012)*, pp. 3459–3464, Institute of Navigation, Tampa, Fla.

World Data Center for Geomagnetism, Kyoto (2014), *Provisional (Quicklook) AE index*, Kyoto Univ., Kyoto, Japan. [Available at http://wdc.kugi.kyoto-u.ac.jp/ae_provisional/index.html, accessed 11 Oct 2014.]

Yeh, K. C., and C.-H. Liu (1982), Radio wave scintillations in the ionosphere, *Proc. IEEE*, *70*(4), 324–360.

Zettergren, M., K. Lynch, D. Hampton, M. Nicolls, B. Wright, M. Conde, J. Moen, M. Lessard, R. Miceli, and S. Powell (2014), Auroral ionospheric *F* region density cavity formation and evolution: MICA campaign results, *J. Geophys. Res. Space Physics*, *119*(4), 3162–3178, doi:10.1002/2013JA019583.